University Library

A gateway to Melbourne's research publications

Minerva Access is the Institutional Repository of The University of Melbourne

Author/s:
Kousal, J;Voermans, JJ;Liu, Q;Heil, P;Babanin, AV

Title:
A Two-Part Model for Wave-Sea Ice Interaction: Attenuation and Break-Up

Date:
2022-05-01

Citation:
Kousal, J., Voermans, J. J., Liu, Q., Heil, P. & Babanin, A. V. (2022). A Two-Part Model for Wave-Sea Ice Interaction: Attenuation and Break-Up. Journal of Geophysical Research Oceans, 127 (5), https://doi.org/10.1029/2022JC018571.

Persistent Link:
https://hdl.handle.net/11343/308318

License:
CC BY

Check for updates

JGR Oceans

RESEARCH ARTICLE
10.1029/2022JC018571

A Two-Part Model for Wave-Sea Ice Interaction: Attenuation and Break-Up

J. Kousal[1], J. J. Voermans[1], Q. Liu[1,2], P. Heil[3], and A. V. Babanin[1]

[1]Department of Infrastructure Engineering, University of Melbourne, Melbourne, Australia, [2]Physical Oceanography Laboratory, Ocean University of China, Qingdao, China, [3]Australian Antarctic Division, Hobart, Australia

Key Points:

- A new model of wave-sea ice interaction, with coupling achieved through wave-induced sea ice break-up based on a nondimensional threshold
- The model is able to capture the position of the unbroken sea ice front and individual break-up events
- The ability of this simple wave model indicates that waves may have a critical influence on Marginal Ice Zone morphology

Supporting Information:

Supporting Information may be found in the online version of this article.

Correspondence to:

J. Kousal,
jkousal@student.unimelb.edu.au

Citation:

Kousal, J., Voermans, J. J., Liu, Q., Heil, P., & Babanin, A. V. (2022). A two-part model for wave-sea ice interaction: Attenuation and break-up. *Journal of Geophysical Research: Oceans*, *127*, e2022JC018571. https://doi.org/10.1029/2022JC018571

Received 20 FEB 2022
Accepted 30 APR 2022

Author Contributions:

Conceptualization: A. V. Babanin
Data curation: J. Kousal, J. J. Voermans
Investigation: J. Kousal
Methodology: J. Kousal, J. J. Voermans, Q. Liu
Resources: A. V. Babanin
Supervision: A. V. Babanin
Writing – original draft: J. Kousal
Writing – review & editing: J. Kousal, J. J. Voermans, Q. Liu, P. Heil, A. V. Babanin

© 2022. The Authors.
This is an open access article under the terms of the Creative Commons Attribution License, which permits use, distribution and reproduction in any medium, provided the original work is properly cited.

Abstract Waves and sea ice form a closely coupled system: waves govern sea ice through stress, floe break-up, and wave-induced currents, while sea ice affects waves through attenuation and reflection. Wave-induced sea ice break-up is particularly important as it can regulate air-sea interaction and consequently also regulate the growth and melt of sea ice. This coupled nature is complex and generally, especially at the large scale, neglected in modeling of the polar climate system. Here, we explore a novel way of coupling through wave-induced ice break-up, and conduct a case study for the Antarctic summer of 2019/2020. Our modeling approach builds upon previous investigations as follows: (a) sea ice takes a binary form, either "broken" or "unbroken," (b) waves may break sea ice, transitioning it from unbroken to broken, (c) a threshold separating breaking and nonbreaking wave fields is used to identify when this occurs, (c) two modes of attenuation for waves in ice (dependent upon the ice state), representing the observed on/off switch in wave attenuation. By characterizing wave attenuation and sea ice break-up as described above, we achieve two-way wave-sea ice coupling, thereby allowing wave-sea ice feedbacks. This model is limited to the ice-melt season as refreeze is not represented here. We demonstrate that our model can simulate both the wavefield in and the evolution of the Marginal Ice Zone. Our results show the validity of empirically derived wave-induced sea ice break-up threshold, and substantiate that waves have a critical influence on the morphology of the Marginal Ice Zone.

Plain Language Summary The interactions between waves and sea ice are complex and, when represented in numerical models, often over-simplified or even neglected. For example, waves act very differently in regions covered by small ice floes or broken ice compared to those covered by an unbroken cover of very large ice floes. Wave dissipation can differ by orders of magnitude, but wave-forecast models usually try to find some "effective" parameters for their attenuation modules valid on average in both environments. Even more, sufficiently large waves can break the ice, thereby changing the behavior of waves in this region. Sea ice forms a crucial barrier between air and sea, and understanding when and how it breaks is crucial to understanding polar regions. Here, we introduce and test a simple yet effective model of wave-ice interaction. Our results show that waves have a critical influence on evolution of sea ice, and are essential to understanding polar regions.

1. Introduction

Waves influence the shape and size of ice floes through ice break-up (Langhorne et al., 1998) and govern the state of initial sea-ice congelation (frazil vs. nilas) and influence its evolution (i.e., pancake ice; Shen & Ackley, 1991). Waves also impart momentum to the ice as they are attenuated (Longuet-Higgins, 1977; Longuet-Higgins & Stewart, 1962), pushing the ice in the direction of wave propagation and affect ice drift (Feltham, 2005; McPhee, 1980; Williams et al., 2017). Stopa et al. (2018) show wave action to be the dominant control of sea-ice translation drift along the outer edge of the Southern Ocean sea-ice area, the Antarctic Marginal Ice Zone (MIZ). There are also numerous indirect effects of waves on ice, such as modified air-sea heat fluxes and enhanced lateral melt associated with break-up of sea ice (Steele, 1992).

Sea ice also governs the wave evolution. Sea ice-induced wave attenuation may be broadly classed into two categories: scattering and dissipation. The former is described by a partial reflection of waves at the boundaries of ice floes, broadening the distribution of wave direction. Scattering by multiple ice edges directly contributes to the exponential decay of the forward-going wave energy. The latter category, dissipation, describes processes which result in loss of energy from the waves. This includes, but is not limited to, internal friction due to ice viscosity, ice fracture (e.g., Squire, 2020), overwash (Toffoli et al., 2015), and under-ice turbulence (e.g., Rabault et al., 2019;

Voermans et al., 2019). The relevance and even more the dominance of each of these processes and categories are essentially unknown. The case studies of Kohout and Meylan (2008) and Montiel et al. (2016, 2018) suggest dissipation to be the more important attenuation mechanism. Within the dissipation framework, Rogers et al. (2021) identified at least three theoretical models consistent with the attenuation observed across a range of conditions. Other studies suggest that dissipation only dominates for long waves, with scattering the dominant attenuative process for short waves (Sutherland & Gascard, 2016; Wadhams et al., 1986).

It is clear that more research is needed on which processes dominate under any given circumstances. In the meantime, we need a workable solution. Many previous solutions have attempted to include all possible physical processes (despite questions regarding their relevance; each often introducing new unknown parameters), with the consequence that our wave-sea ice interaction models have become burdened with increasing complexity and more unknowns. These unknowns are often used as tuning parameters, meaning such empirical models will need to be re-run each time the wave or ice conditions change, thereby limiting their broader relevance.

Many previous solutions also neglect two-way coupling between waves and sea ice. As soon as we have both waves and sea ice evolving together, it is insufficient to only consider the effect of waves on ice, or of ice on waves. The case studies of Collins et al. (2015) and Ardhuin et al. (2020) both show a rapid evolution of waves and sea ice over the period of a few hours, with the sea ice breaking in response to the waves, and the waves within the sea ice rapidly growing in response to this changed ice state. Both report two distinct phases in attenuation of waves by sea ice: strong attenuation under unbroken ice conditions, and unimpeded propagation under broken ice conditions. Wave attenuation reduces by at least an order of magnitude once the ice is broken (Voermans et al., 2021), hence the waves can propagate further and break more sea ice.

Interactions between waves and sea ice carry implications for many other aspects of the polar climate. For example, when the sea ice breaks there is a direct connection between ocean and atmosphere, meaning heat fluxes can transfer between the two. In the ice melt season (typically warm air), sea ice break-up leads to a warming of the ocean surface and a consequent acceleration of ice melt, including lateral melting (Bateson et al., 2020; Boutin et al., 2020). This melting is further accelerated by the decrease in albedo (and resultant increase in solar radiation absorbed) due to the exposure of dark ocean below the ice (Curry et al., 1995). As a result, there is more open water, waves can have longer fetches and grow higher, and further break the weakened ice in MIZ (Thomson & Rogers, 2014). Li et al. (2021) shows that this wave-induced sea ice break-up can accelerate melting in this season. In the ice growth season (typically cool air), sea ice break-up leads to a rapid cooling of the ocean surface, enabling the surface to refreeze during calm periods after the ice floes spread to larger areas, thereby suppressing wave generation and attenuating incoming waves. Li et al. (2021) shows that this wave-induced sea ice break-up can lead to increases in sea ice concentration and thickness in this season.

Insufficient knowledge regarding the underlying physics (as well as the additional complications brought by high-complexity solutions) act as motivation for a relatively simple solution to this issue, but one that still addresses the coupled nature of waves and sea ice. Here, we introduce and test such a solution: a new simple coupled model which treats sea ice mechanical integrity as binary—either "unbroken" or "broken." This binary approach is motivated by the aforementioned two-phase attenuation reported by Collins et al. (2015) and Ardhuin et al. (2020). We represent this two-phase attenuation by introducing a partition into the simple two-layer dissipative attenuation model of Sutherland et al. (2019). The binary switch in our model is given by the critical threshold of the ice-breakup parameter of Voermans et al. (2020). Although simple, we show in this study that our model can capture the coupled nature of the wave-sea ice system through characterization of the critical feedback between ice-induced wave damping and the wave-induced sea ice break-up.

2. Methods

A nested version of the third-generation spectral wave model, WAVEWATCH-III, is used (hereafter WW3; WW3DG, 2019). Wave information is passed from the global coarse-resolution grid (0.5° or approximately 50 km) to the Davis Sea (East Antarctica) regional high-resolution grid (0.1° or approximately 10 km; Figure 1). The global grid domain is unbounded in longitude (with circular boundary conditions) and bounded by 80°S–80°N, while the Davis Sea grid domain is bounded by 60°−80°E and 70°–60°S. The default coastlines database in WW3 is the Global Self-consistent, Hierarchical, High-resolution Geography Database (GSHHG; Wessel & Smith, 1996). GSHHG is used for the global grid, whilst the Scientific Committee on Antarctic Research

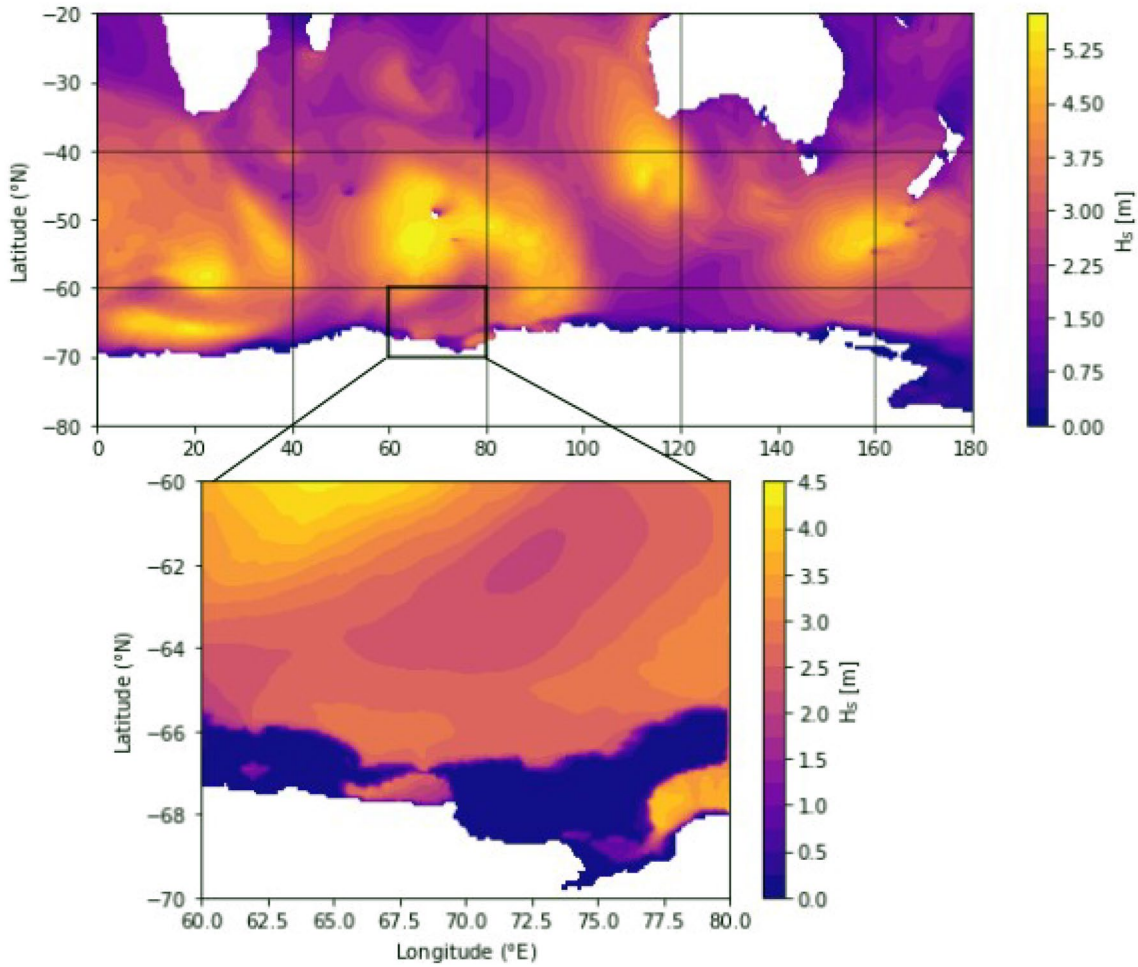

Figure 1. A nested set-up of WAVEWATCH-III. Wave information is passed from a global coarse-resolution grid (0.5°) to a Davis Sea regional high-resolution grid (0.1°). Snapshot of significant wave height (H_S) at 00:00, 9 January, 2020.

Antarctic Digital Database (SCAR ADD; Scientific Committee on Antarctic Research, 2000) coastlines are used for the Davis Sea grid. This latter database is used for its higher accuracy in Antarctic regions. The global model is forced with 0.5° sea ice concentration and 10 m-wind fields from ECMWF's ERA5 reanalysis. The Davis Sea model is forced with 0.1° wind fields from ECMWF's archived forecasts, and high-resolution (3.125 km) AMSR2 satellite data for ice concentration (Beitsch et al., 2013 updated). For both grids, frequency resolution increases by factor 1.1, with the first frequency at 0.045 Hz, and 30 frequency bins. There are 36 directional bins (each 10°). Time step information is summarized in Table 1.

Table 1
Time Step Information for the Davis Sea and Global WW3 Grids

Grid	DTMAX	DTXY	DTKTH	DTMIN
DAVIS SEA	450s	225s	225s	10s
GLOBAL	1800s	900s	900s	10s

Note. DTMAX is the maximum global time step, DTXY is the maximum Courant–Friedrichs–Lewy (CFL) time step for x-y, DTKTH is the maximum CFL time step for spectral advection, and DTMIN is the minimum source term time step.

For representation of sources and sinks of wave energy, we use the source term package ST6 (Liu et al., 2019). This source-term package represents the physical processes of wind-wave interaction, whitecapping (dissipation due to breaking) and wave-turbulence interaction (swell dissipation), and has its roots in field and laboratory observations and experiments. CDFAC, the ST6 parameter to account for wind field biases, is set to CDFAC = 1.08 as in Liu et al. (2021).

The global grid is run from 22 November 2019 to 14 February 2020, and the Davis Sea grid is run from 13 December 2019 to 14 February 2020. Both grids are initialized with the JONSWAP spectrum (Hasselmann et al., 1973).

Table 2
Model Simulations

Label	Young's modulus, Y (GPa)	Flexural strength, σ (MPa)	Ice thickness, h_i (m)	Attenuation reduction coefficient for broken ice, β ( )
A	9	0.1	0.55	0.01
B	9	0.1	1.1	0.01
C	6.0	0.55	1.1	0.05
D	0.2	0.7	1.1	0.1
E	0.2	0.7	2.2	0.1

Note. All simulations begin 27 December 2019 and finish 14 February 2020. Attenuation increases in strength from simulation A through E.

The first month of data is discarded for the global grid, as are the first 2 weeks for the Davis Sea grid to ensure adequate model spin up time.

To describe wave attenuation through the sea ice, we use the relatively simple two-layer attenuation model of Sutherland et al. (2019; hereafter SEA19). This is a dissipative model in which wave energy is lost to internal friction within the sea ice. The attenuation through the sea ice for SEA19 is described by

$$\alpha_{\mathrm{SEA19}} = \frac{1}{2}\Delta_0 \epsilon h_i k^2 \tag{1}$$

where Δ_0 determines the boundary condition at height $-(1-\epsilon)h_i$, h_i is sea ice thickness, k is wave number, $\Delta_0 = 1$ (no-slip condition), and $0 \le \epsilon \le 1$ (relative thickness of the high-viscosity layer). Note, attenuation here follows a power dependence on frequency of $n = 4$ ($k \sim f^2$), in fitting with the range reported by Rogers et al. (2021) of $n = 2$ to 4.

To account for the binary nature of wave-sea ice interaction, we distinguish two regimes in the SEA19 model:

$$k_i^{\mathrm{IBT}} = \begin{cases} k_i^{\mathrm{IBT}}{}_{\text{unbroken ice}}: \ \alpha_{SEA19} \\ k_i^{\mathrm{IBT}}{}_{\text{broken ice}}: \ \beta\alpha_{SEA19} \end{cases} \tag{2}$$

where k_i^{IBT} is the imaginary part of the wave number representing wave growth/decay, β represents the attenuation reduction for broken sea ice (relative to unbroken sea ice cover), with $0 < \beta < 1$. The model is initialized with all sea ice as unbroken, meaning we are in the $k_i^{\mathrm{IBT}}{}_{\text{unbroken ice}}$ attenuation regime. To determine when the sea ice breaks, we use the non-dimensional sea ice-breakup parameter of Voermans et al. (2020; hereafter VEA20)

$$I_{\mathrm{br}} = \frac{a h_i Y}{\sigma \lambda^2} \tag{3}$$

where a is wave amplitude (approximately equal to half of the significant wave height), h_i is sea ice thickness, Y is Young's modulus, σ is flexural strength and λ is wave length. The sea ice at any point is classed as "broken" when I_{br} exceeds its critical threshold,

$$I_{\mathrm{br\_crit}} = 0.014 \tag{4}$$

thereby resulting in a transition to the "broken ice" attenuation regime, $k_i^{\mathrm{IBT}}{}_{\text{broken ice}}$. Assuming that the ice does not refreeze (a valid assumption for this time of year), this point then remains in the "broken ice" attenuation regime for the remainder of the simulation.

Built upon these, we have run five simulations with our new model. A conservative range for Y and σ was chosen to describe the full range of sea ice material properties, with $\sigma \in [0.1, 0.7]$ MPa and $Y \in [0.2, 9]$ GPa (Karulina et al., 2019; Timco & Weeks, 2010). The range for the attenuation reduction coefficient for broken ice is $\beta \in [0.01, 0.1]$ (Voermans et al., 2021). Here, we choose $\beta = 0.05$ as being the median value. The simulations, detailed in Table 2, are based on the combinations that result in the largest range of physical behavior. The range of model behavior between the "outer upper bound" (A) and "outer lower bound: (E) is referred to as the model's outer physical range, while the range between the "inner upper bound" (B) and "inner lower bound" (D) simulations we refer to as the model's inner physical range. The ice thickness for the inner physical range is based on a field measurement performed at the time of instrument deployment (Voermans et al., 2020). The outer physical range includes a modification to this to account for the possibility of thicker/thinner sea ice throughout other regions of the domain. The upper (lower) bounds refer to behavior of significant wave height (H_S), and correspond with lower (higher) wave attenuation and less (more) unbroken ice. Simulation C is our baseline simulation, with the sea ice parameters used being approximately in the middle of their physical ranges.

To calibrate and verify WW3, we use the data described in VEA20: two ice motion loggers (Rabault et al., 2020; hereafter denoted IB) and two wave buoys (Spotter buoys from Sofar Ocean Technologies; hereafter denoted

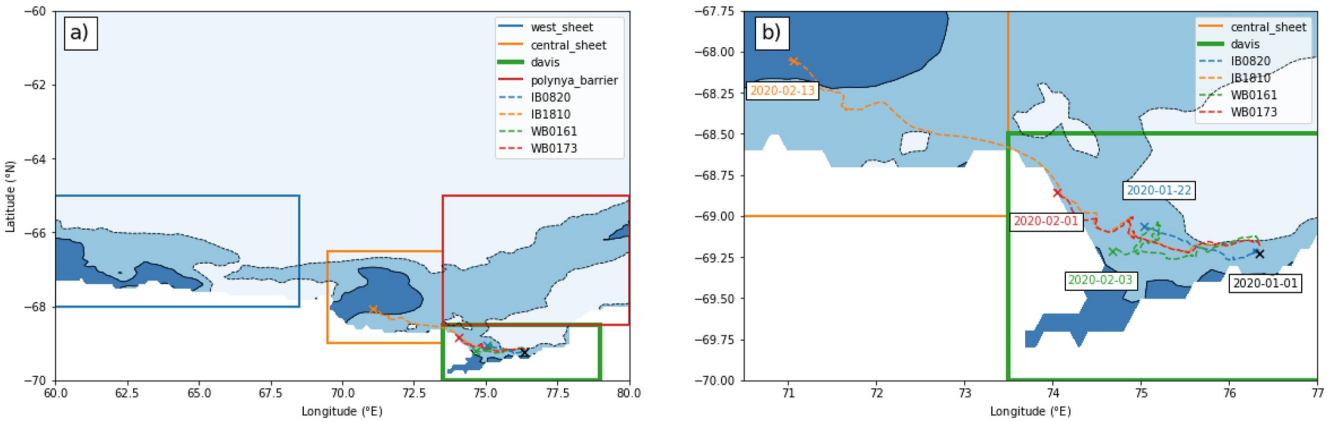

Figure 2. Domains and buoy tracks of the model domain (a), and a close-up of the buoy tracks (b). Crosses and text indicate position and date of last transmission. Dashed and solid black lines mark 15% and 85% sea ice concentration (SIC) contours respectively from the AMSR2 satellite SIC product (average between 1 January and 14 February). Light blue indicates <15% SIC, medium blue indicates 15% to 85% SIC and dark blue indicates >85% SIC.

WB). Both IB and WB transmit integrated wave parameters (e.g., H_S and f_p) and wave energy density. The accuracy of the observed significant wave height is of the order of a centimeter, but varies with wave frequency (the reader is referred to Rabault et al., 2020 and Voermans et al., 2020 for more details). The instruments were deployed on landfast ice in the Davis Sea in December 2019, along a transect perpendicular to the landfast ice edge. The first instrument was deployed about 100–200 m from the edge, and subsequent instruments were deployed a few kilometers apart. Instruments started to drift after a breakout event on the second of January. The instrument tracks are shown in Figure 2, with the text denoting the times of their last transmissions. Note that IB1810 continued to transmit beyond 14 February 2020, the end of our study period.

3. Results

Wave and wind climate in the Davis Sea is dominated by passing low-pressure systems in the nearby Southern Ocean, with a storm passing by approximately once every week. The first significant storm in this study is on January 8. Using the 2 day period over which all buoys show significant wave activity (8–10 January), we calibrate the model to observations of H_S within the MIZ. This is achieved through the adjustment of ϵ (relative thickness of the highly viscous ice layer; see Equation 1). $\epsilon = 1.2e - 2$ is determined as the optimal value (see Text S1 in Supporting Information S1 for details). Using this value, our model is then able to simulate wave behavior throughout the MIZ over the complete simulation period (27 December 2019–14 February 2020).

Our baseline simulation (C) captures the timing of wave events well, with peaks in H_S occurring at the same time as those observed by the buoys (Figure 3). Its ability to accurately capture the magnitude of these peaks differs vastly between wave events, and sometimes even between different buoys for the same event. For the small wave activity on January 5, simulation C closely matches the observations for all buoys. For January 7, we see an increase in wave size at WB0161 and WB0173, but not IB0820 and IB1810. Simulation C well represents the wave activity of these latter two buoys, but under-represents the wave activity of the former two. For the large event on January 9, we see accurate representation for buoys IB1810 and WB0161, but a slight over-representation for IB0820, and a considerable under-representation for WB0173. For the observed peak on January 29, simulation C captures the wave activity at WB0161, but under-represents wave size at buoys IB1810 and WB0173. From January 29 on-wards, we observe a marked increase in wave activity (this is due to a loss of sea ice to the north of the Davis Sea not shown here). For the large wave activity observed on February 1 to February 3, simulation C accurately captures the wave activity at IB1810 and WB0161 (apart from a brief under-representation on January 1). From February 5 to February 9, simulation C accurately follows the observations at buoy IB1810 with the exception of two short spikes (February 6, February 8). These short-lived spikes are due to model discretization: the buoy is close to the border of the adjacent cell here (which is one cell less deep into the MIZ and therefore the waves here have been less heavily attenuated) and briefly enters it twice causing spikes in wave size tracking the buoy. There is then another peak in observed waves at IB1810 which simulation C under-represents (January 10), after which the simulation shows similar wave activity as observed by IB1810 (January 11–14).

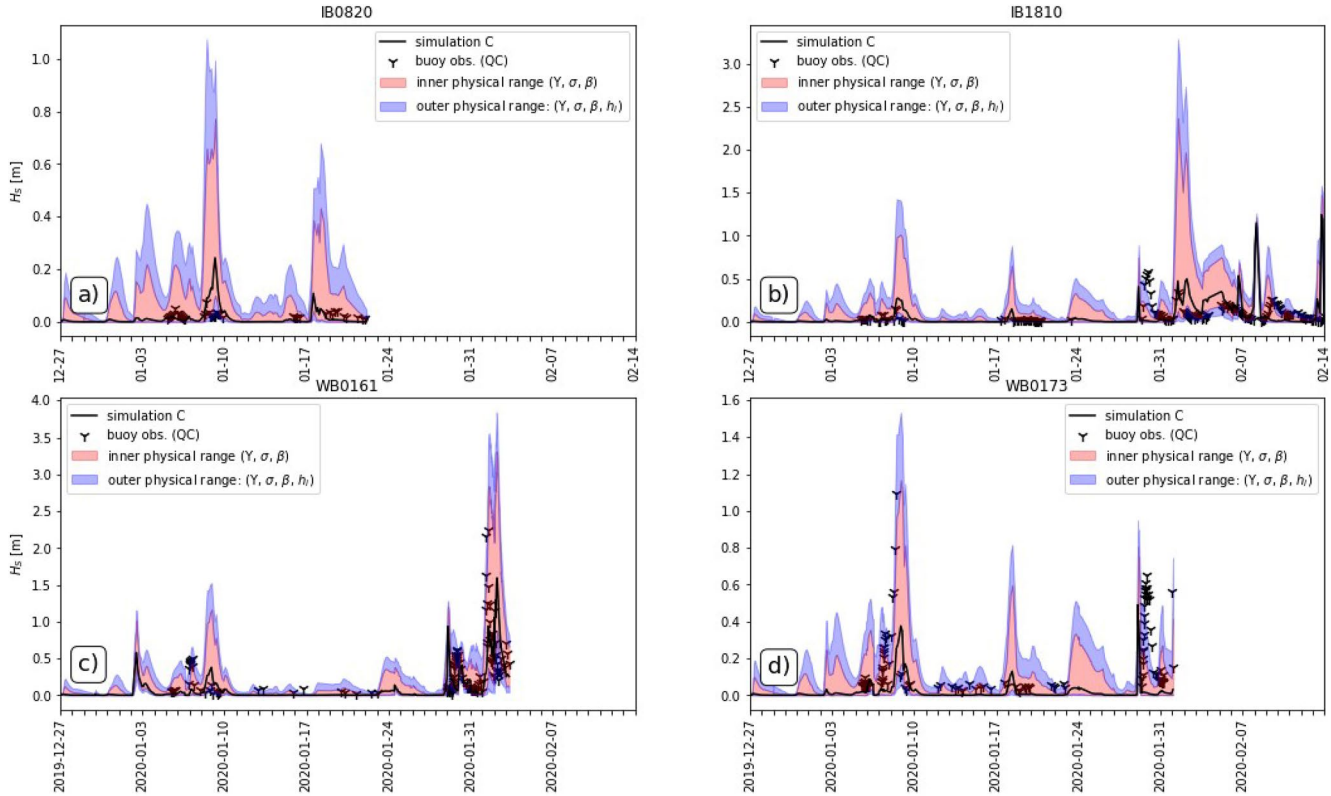

Figure 3. Modelled and observed significant wave height (H_S) following the buoys. Black markers indicate quality controlled onboard buoy H_S calculations. The inner (outer) physical range is defined as the range between the inner (outer) upper and lower bounds (see Table 2 for simulation details).

The difficulty for our baseline simulation (C) in consistently matching the observations is partly rooted in the highly heterogeneous nature of the ice field. The range in wave behavior spanned by the additional simulations account for this heterogeneity (Table 2). The H_S range spanned by our inner physical range (simulations B and D) captures the vast majority of observed H_S values. The H_S range spanned by our outer physical range (simulations A and E) captures the remainder, with one exception: January 29. The observations at buoys IB1810 and WB0173 on this day exceed the maximum of the outer physical range by approximately 0.1 m (approximately 20% of the peak). This is most likely due to weaker/thinner sea ice in the path from the ocean to the buoy than accounted for in the outer physical range. Note that this exceedance is not seen at the other buoy still active at this time (WB0161). Figure 4 shows the energy-frequency spectrum for WB0173 on January 30 (modeled and observed). We see that simulation C captures the distribution of this energy very well, and that all observations fall entirely within the inner physical range. Thus, our results show confidence that the developed model can replicate the field observations within reasonable accuracy using the inner physical range.

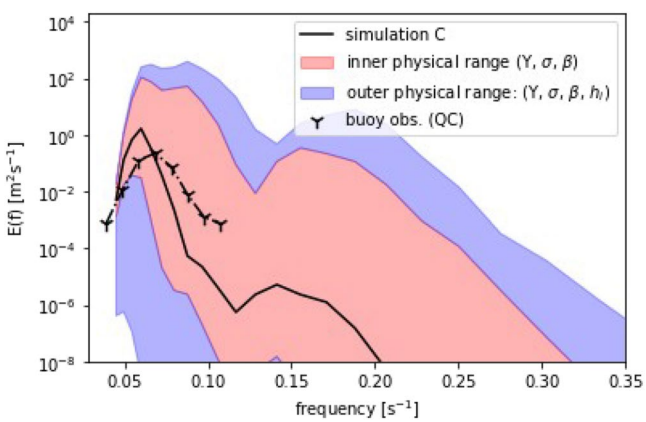

Figure 4. One-dimension modelled and observed wave spectra. Buoy observations shown by crosses. Buoy location for 01 February can be seen in Figure 2. The inner (outer) physical range is defined as the range between the inner (outer) upper and lower bounds (see Table 2 for simulation details). Buoy: WB0173; time: 2020-01-30T06:48.

3.1. Davis

Figure 5a shows the number of grid points with unbroken ice in the Davis Sea throughout the study period (equivalent to total area coverage of unbroken ice), consisting of long periods of stability punctuated by short periods of rapid decline. Note that there are no increases in unbroken ice area due to the "no refreeze" assumption. Recalling that the study period is characterized by sea ice retreat, this downwards trend in unbroken ice is logical. There is an inverse relationship between unbroken ice area and system stability, with the

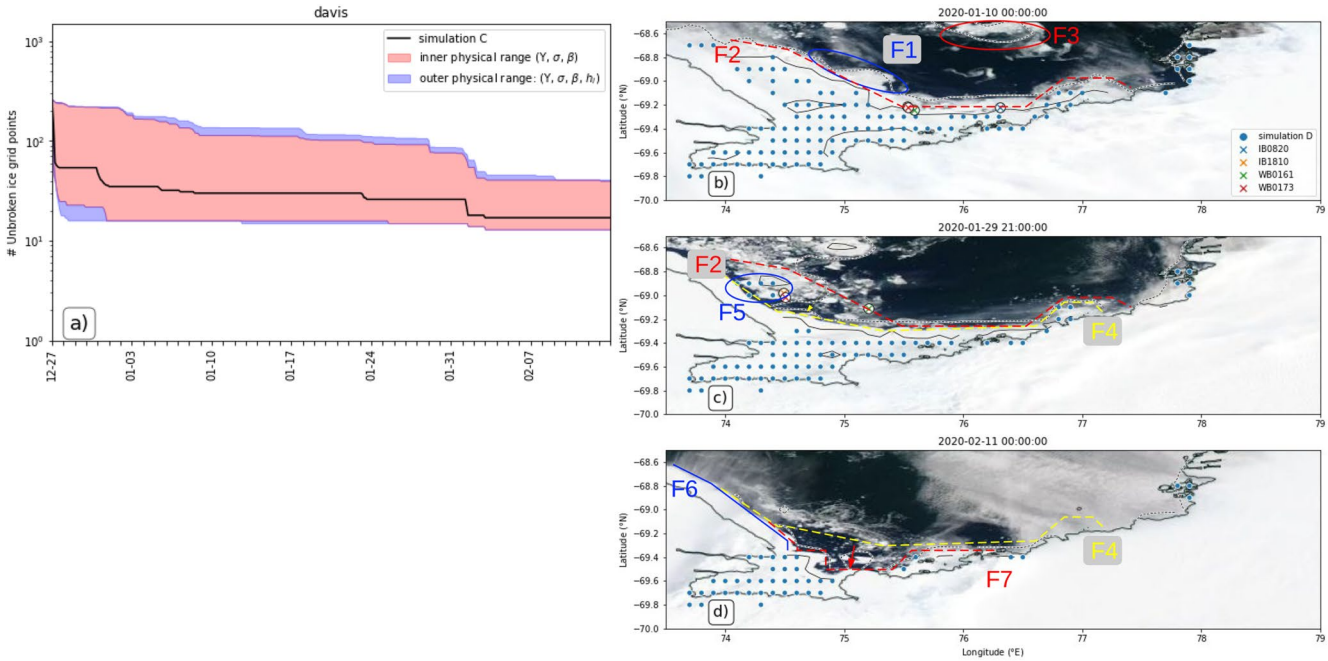

Figure 5. (a) Modelled number of unbroken ice grid points for the Davis Sea region. The inner (outer) physical range is defined as the range between the inner (outer) upper and lower bounds. See Table 2 for simulation details. (b–d) Model simulations of unbroken sea ice for the Davis Sea region. Blue dots mark modelled solid ice for the inner upper physical bound (simulation D; see Table 2 for simulation details). Dashed and solid black contours mark lines of 15% and 85% sea ice concentration respectively. Buoy locations are shown by the coloured crosses. Corrected Reflectance satellite imagery from the MODIS satellites are shown (https://worldview.earthdata.nasa.gov). The colour of the "F-numbers" refers to the lines of the same colour and are to be discussed in the text.

upper bounds for unbroken ice (simulations D and E) showing more frequent and larger break-up than the lower (simulations A and B), which remain virtually constant, with approximately 20 cells of unbroken ice. Simulations D and E evolve from approximately 300 cells to just 40 by the end of the study period. This enhanced stability for the simulations A and B may be explained by a large barrier of broken ice (weakly attenuating the waves) shielding the unbroken ice from wave-induced break-up.

Figures 5b–5d show the geographic distribution of the simulated unbroken ice for January 10, January 29 and February 11. Simulation D is the upper bound of the inner physical range with respect to unbroken ice. This simulated unbroken ice is superimposed onto satellite imagery (MODIS) for the corresponding days. The dates are selected to understand the spatial nature of the ice loss observed in Figure 5a and to verify the simulated ice break-up. This verification relies on MODIS to differentiate between unbroken and broken ice. The MODIS satellite operates on the visible part of the electromagnetic spectrum, from which it can be difficult to determine features of the unbroken ice, such as sheet boundaries, unless bordered by ocean (the dark color provides a strong contrast). Figure 5c shows an example of a sheet boundary bordered by ocean, where the boundary between ocean and the land-fast sea ice is clearly visible in MODIS (F1 in Figure 5). We assume that boundaries like this mark the extent of the unbroken ice. Simulation D shows unbroken ice extending to this edge (F2). We can also use MODIS to distinguish (e.g., F3).

The unbroken ice edge in simulation D has retreated by January 29, particularly on the north-west face of the sheet (F4), with this ice loss being attributed to the aforementioned January 23 break-up event (Figure 5a). MODIS corroborates this loss of unbroken ice in this region, with the MODIS ice fragmented where before it was continuous (between F2 and F4). The unbroken ice in simulation D continues to follow the boundary of MODIS closely (F4), with the exception of a slight high bias at 74.5°E, 69°S (F5). It is worth drawing to the reader's attention the "unbroken" ice stretch at 74°E, 69°S (F6). This is not unbroken sea ice, but rather part of the ice shelf. This is a study focused on sea ice, and this shelf ice is therefore not represented within our model.

The unbroken ice in simulation D has retreated further by February 11, most evident at 75°E, 69.5°S (F7). The aforementioned high bias at 74.5°E, 69°S has disappeared. These ice losses can be attributed to the February

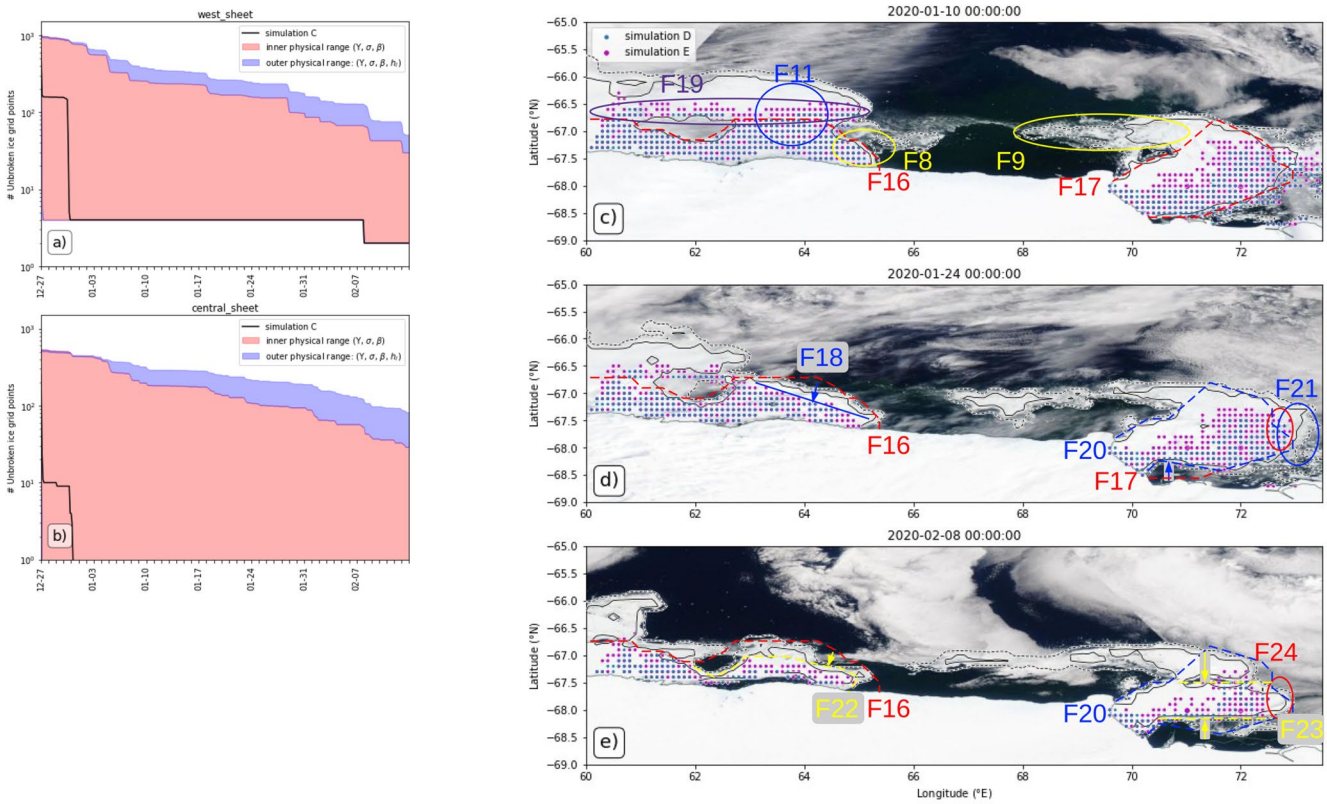

Figure 6. (a, b) Modelled number of unbroken ice grid points for the western and central sheets. The inner (outer) physical range is defined as the range between the inner (outer) upper and lower bounds. See Table 2 for simulation details. (c–e) Model simulations of unbroken sea ice for the western and central sheets. Blue and magenta dots mark modelled solid ice for the upper physical bounds (simulations D and E; see Table 2 for simulation details). Dashed and solid black contours mark lines of 15% and 85% sea ice concentration respectively. Buoy locations are shown by the colored crosses. Corrected Reflectance satellite imagery from the MODIS satellites are shown (https://worldview.earthdata.nasa.gov). The color of the "F-numbers" refers to the lines of the same colour and are to be discussed in the text.

1 break-up event (Figure 5a). MODIS corroborates this loss of unbroken ice at 75°E, 69.5°S, with this part of the ocean now ice free (between F4 and F7). Again, the unbroken ice in simulation D follows the boundary of MODIS closely (F7).

3.2. Western and Central Sheets

The time series of the unbroken ice amount for the western and central sheets show similar features to that of the Davis Sea, namely prolonged periods of relative stability punctuated by short periods of rapid decline, and a greater stability for the lower bound simulations with respect to unbroken ice, with the upper bounds slowly converging toward them (Figures 6a, 6b). There is more unbroken ice in the western and central sheets relative to the Davis Sea, with the upper bounds beginning respectively at 1,000 and 600 cells of unbroken ice, compared to the 300 of the Davis Sea. Note that the lower bounds for these regions consist of virtually no unbroken ice. For the central sheet, this happens instantly, whereas we see a few remnant cells of unbroken ice persist in the western sheet. The Davis Sea region was probably able to maintain more unbroken ice in the lower bound due to geographical (and ice field) wave protection. Also note that the ice loss in the central sheet consists of highly frequent but small break-up events, whilst it is less frequent but larger for the western sheet. This is also likely a due to protective difference resulting from a combination of the surrounding geography and ice field. The ice loss in the Davis Sea region is more similar to the western sheet in terms of frequency versus magnitude.

Figures 6c–6e show the geographic distribution of the simulated unbroken ice for January 10, January 24 and February 8 (simulation D; the upper bound of the inner physical range) overlaid onto MODIS. The dates are slightly different to those of the Davis Sea analysis due to cloud cover interference. Beginning with January 10, we see a clear boundary in MODIS for much of the western and central ice sheets (e.g., F8). There is additional

ice attached to these sheets which can be identified as broken ice (e.g., F9). It is somewhat ambiguous in some regions where the unbroken ice stops and the broken ice begins (e.g., F11). Here, we use supplementary MODIS images to help determine the likely extent of the unbroken ice. In Figure S2 in Supporting Information S1, we highlight cracks/fragmentation in the ice that are not as clearly visible in Figure 6 for the western sheet (F12 and F13 in Figure S2 in Supporting Information S1), allowing us to determine the likely extent of unbroken ice (F16 in Figure 6). The unbroken ice in simulation D (the blue dots) follows this boundary from MODIS very well (F17). The central sheet appears to consist entirely of tightly packed broken ice (F14 in Figure S2 in Supporting Information S1) with the exception of one large ice floe (which may be an ice berg calved from the ice shelf rather than being sea ice; F15). Note that this violates the initial assumption of the model that all sea ice is initially unbroken. The analysis of the central sheet will therefore proceed with the acknowledgment that this is tightly packed broken ice and not unbroken sea ice.

It is important to stress that the ice thickness used for the inner physical range simulations was only measured at the deployment site of the instruments (Davis Sea) and is therefore unlikely to be representative for the Western and Central Sheets. We therefore also show the results of simulation E in Figure 6 (unbroken ice market by the magenta dots), which considers an ice thickness double that of simulation D. With respect to simulation D, an increased ice thickness increases the extent of unbroken ice for both the central and western sheets. This increase of unbroken ice present an interesting contradiction to the employed ice break-up threshold (Equation 3), which states that the ice break-up, I_{br}, increases with ice thickness. As ice thickness increases however, so too does attenuation (Equation 1), thereby decreasing the wave energy passing through the MIZ and subsequently available for the potential break-up of sea ice.

Although simulation D shows a significant contraction of the north eastern edge of the western ice sheet from January 10 to January 24 (F18), the unbroken ice in MODIS appears to maintain relatively stable over this period, essentially following the same contour as previously (F16; Figure 6d). This model ice loss (F18), largely occurring on January 18 (Figure 6a), has resulted in another low bias, now in the western sheet. Simulation E, with its thicker ice and reduced ice retreat, reduces this bias, but does result in a slight high bias in northerly extent of this ice sheet for January 10, however (F19), not yet registering the northern part of this sheet yet as broken. Considering that we used images from January 12 and 13 (Figures S2a, S2b in Supporting Information S1) to diagnose the extent of the unbroken ice here (due to cloud cover), it is also possible that this ice in reality has not yet broken, and that the model is accurately representing the extent of unbroken ice here. We also see a retreat of the tightly packed broken ice in the central sheet on the southern border (MODIS; F20). The model shows similar ice loss on the southern boundary, as well as additional ice loss on the eastern boundary (F21).

Over the next 2 weeks (January 24–February 8), we see further contraction of the western sheet in both MODIS and model (F22). By February 24, simulation E closely follows the MODIS unbroken ice here, while simulation D maintains a low bias. MODIS shows significant losses incurred by the tightly packed broken ice in central sheet over this period. This consists of a large region detaching in the north, as well as some further losses to the southern boundary (Figure 6f; F23). Similar to the losses seen in MODIS (F23), the model shows ice retreat for the northern and southern boundaries, as well as some additional losses incurred to the eastern boundary (F24).

3.3. Polynya Barrier

The fourth region is the polynya barrier. For the time series of unbroken ice, we see the same model characteristic features as previously (Figure 7a): prolonged periods of relative stability punctuated by short, rapid declines, and greater stability for the lower bounds with respect to unbroken ice, with the upper bounds converging toward them. The lower bounds fall to zero cells of unbroken ice instantly; the upper bounds begin with 500–600. The ice loss here is more similar to the Davis Sea and western sheet in terms of frequency versus magnitude of ice loss (less frequent, larger losses). Different here, however, is that all simulations have converged to zero unbroken ice by January 29, indicating very high confidence that the wave energy is sufficiently large to break all ice.

Figures 7b, 7c shows the geographic distribution of the simulated unbroken ice for January 10 and January 24 (simulation D) overlaid onto MODIS. MODIS shows ice across the entirety of this region as broken. Simulation D, however, still shows some unbroken ice remaining here in the center of the ice pack (F25). This unbroken ice is consumed by January 23 (Figure 7a,c).

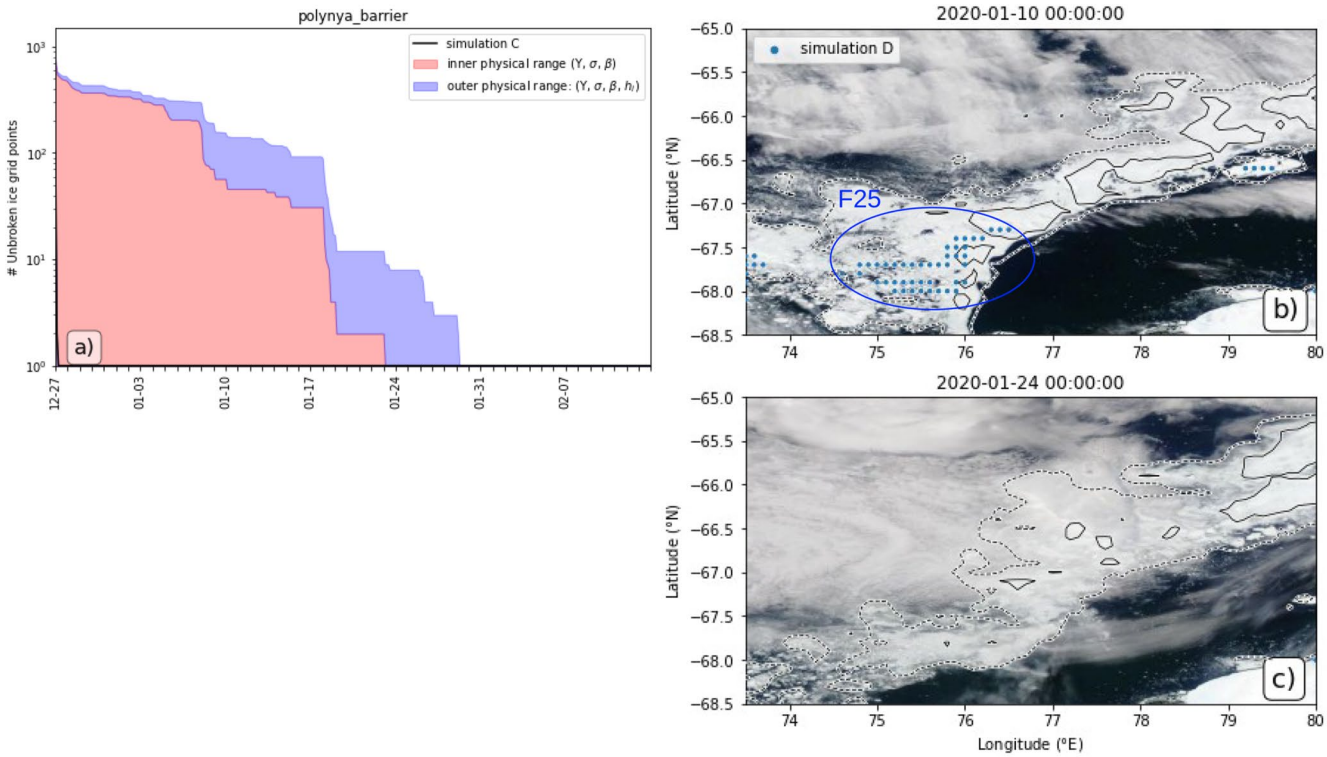

Figure 7. (a) Modelled number of unbroken ice grid points for the polynya barrier. The inner (outer) physical range is defined as the range between the inner (outer) upper and lower bounds. See Table 2 for simulation details. (b, c) Model simulations of unbroken sea ice for the polynya barrier. Blue dots mark modelled solid ice for the inner upper physical bound (simulation D; see Table 2 for simulation details). Dashed and solid black contours mark lines of 15% and 85% sea ice concentration respectively. Buoy locations are shown by the colored crosses. Corrected Reflectance satellite imagery from the MODIS satellites are shown (https://worldview.earthdata.nasa.gov). The color of the "F-numbers" refers to the lines of the same colour and are to be discussed in the text.

4. Discussion

Here, we present a novel wave-sea ice interaction model applied to an Antarctic case study. We verify the model's performance first with respect to wave properties, and second with respect to the two-phase ice field (unbroken and broken). The model performs reasonably well in replicating the observations of waves in sea ice in the Davis Sea. Discrepancies between model and observations are largely caused by the highly spatial heterogeneous composition of the sea ice (i.e., Figures 5–7). Specifically, the distance of the instruments to the landfast ice edge (and notably, the ice edge is adjacent to the polynya) is similar in magnitude as the grid resolution of the model, causing properties to vary greatly between neighboring cells. This ultimately means that the calibration and validation of wave properties is very sensitive to the definition and discretization of the model grid and model input, and the exact position at which the instrumentation is located with respect to the grid. The impact of the strong spatial variability of the ice cover can be observed in the model output and in situ observations in up to January 10, where the instruments are within close proximity of each other, nevertheless, present a substantially different significant wave height (Figure 3). Given the major challenges in the modeling of waves in ice in this specific study, the comparison of the simulated wavefield against the in situ observations is very positive (Figures 3 and 4).

There are four assumptions made in this study which require some discussion with respect to their justification and/or implications: (a) ice thickness, strength and elasticity are homogeneous in space and time. While this is typical practice in the current state of the field due to difficulty of obtaining information of sea ice properties at vast scales, it is a limitation which hinders the reliability of the simulation across large geophysical scales and long time duration. We see a substantial difference in results for both wave attenuation and ice break-up when the complete physical range of the ice properties are considered; (b) sea ice cannot transition from its "broken" state to a "unbroken" state (i.e., no refreezing is allowed). We consider this a reasonable assumption considering the season of the simulations but note that such assumption is likely invalid when temperatures become lower;

(c) unbroken ice is geographically anchored (i.e., does not drift). The unbroken sea ice identified by our model appears to be primarily land-fast sea ice and, according to MODIS, does not appear to be drifting. The unbroken sea ice in the polynya barrier, however, is not land-fast, but breaks up so rapidly that this is not a concern; (d) dissipation is the dominant mechanism for attenuation of waves in ice. This is a valid assumption for the long waves characteristic of this region, but may be invalid where shorter waves are more dominant (e.g., some regions of the Arctic) as scattering may dominate (Sutherland & Gascard, 2016; Wadhams et al., 1986).

We believe this model to be of general interest to the field of wave-sea ice interaction for the following reasons: (a) the threshold used here for sea ice break-up was developed across a diverse variety of ice scales, meaning that the model is not limited to a specific location/scale, (b) the attenuation model within our model can effectively be considered a generic dissipative model with a power-4 frequency dependence ($k \sim f^2$) and a single calibration coefficient, meaning we are not carrying any assumptions about the dominant relevant physical attenuative processes (apart from attenuation following a power-4 frequency dependence in fitting with the range reported by Rogers et al., 2021).

The proposed model has significant potential to be embed coupled wave-ice processes in polar modeling more generally. While the MIZ evolution can be modeled satisfactorily by wave-sea ice interaction alone as shown in the presented case study, this model could be extended to scenarios in which winds and currents may play a more significant role, provided that a model for sea ice propagation/drift is coupled to the existing model. This drift model must have two separate regimes: one for unbroken sea ice where the ice is one continuous sheet and not subject to divergence, and one for broken sea ice in which divergence is allowed. Furthermore, if we choose a coupled sea-ice model such as CICE for this purpose, we could then use information from this model to relax assumptions (a) and (b) outlined above: thickness, strength and elasticity could be calculated from ice model (a), and broken sea ice could refreeze according to the sea-ice model thermodynamics (b).

There is no straightforward method available to validate the simulated two-phase ice field and we had to resort to visual analysis using MODIS satellite imagery. Despite the subjectivity of this approach and the simplicity and limitations of the model, the performance of our model in identifying regions of broken and unbroken ice is satisfactory. A major source of error between the simulations and the observations is that the wave-ice coupled model only considers break-up induced by waves while other processes, including wind and currents, have the capacity to break the ice as well. Aside from the uncertainty in sea ice material and physical properties, the exclusion of these break-up mechanisms can, in part, explain why sections of the sea ice are considered unbroken by the model, but appear as broken in the satellite images. Additionally, parts of the ice cover may have been broken prior to the study period, and remain so, potentially causing a bias later in the simulations if the waves are not strong enough to break this ice at a later stage in the simulation. We see this bias manifestation for the central sheet, where there remains a considerable amount of unbroken ice in the model, despite the region consisting of broken ice from the beginning (as shown by MODIS). The polynya barrier region shows the opposite case: despite the discrepancy between the model assumption (all ice initially unbroken) and reality (all sea ice broken as shown by MODIS), the model is able to provide a realistic representation of sea ice for the study period.

The strong correspondence between the simulated two-phase ice cover and satellite imagery substantiates the capacity of waves to influence the sea ice morphology in the MIZ and at very short time scales. This identifies the importance of two-way coupling of waves and sea ice for accurate prediction in forecasting models. Further studies are, however, required to assess model performance at different sites, preferably at sites where more details are available on the mechanical properties of the ice and ice thickness.

5. Conclusions

This study presents a new simple wave-sea ice coupled model, and applies it to a case study in the Antarctic over the summer of 2019/2020. Our model can be summarized as follows: (a) sea ice takes a binary form, either "broken" or "unbroken," (b) waves can break sea ice, transitioning it from unbroken to broken, (c) the threshold of Voermans et al. (2020) is used to identify when this occurs, (d) there are two modes of attenuation for waves in ice (dependent upon the ice state), representing the on/off attenuation reported in Collins et al. (2015) and Ardhuin et al. (2020), (e) through the attenuation and ice break-up described above, we achieve two way wave-sea ice coupling, thereby allowing wave-sea ice feedbacks. We note here that this study is the first to implement observation-based features (c) and (d) within a numerical wave model. We use in situ buoy observations to validate

the modeled waves, and satellite imagery to validate the modeled sea ice. The model is run for a variety of ice properties to understand the range of possible physical behavior of the system.

The baseline simulation (C) captures the timing of wave events but, due to the spatial heterogeneity of the ice field, has some trouble in accurately capturing the magnitude of the waves at each buoy. We account for this spatial heterogeneity here by varying the mechanical properties of the ice within a likely physical range, allowing us to capture the full range of wave behavior observed by the buoys. This accuracy of the model holds true not just for significant wave height, but also for the spectral distribution of wave energy.

We note an inverse relationship between quantity of unbroken ice and system stability, with systems with more ice being prone to more frequent and larger break-up events. This is likely due to the shielding afforded to the unbroken ice by the broken ice surrounding. Using satellite imagery for verification, we also demonstrate the model's high ability to represent sea ice break-up (and consequently the two-phase sea ice field), accurate in both the spatial and temporal dimensions. The accuracy of this model also substantiates the ability of the observation-based features of a binary sea ice state (unbroken/broken) with associated on/off attenuation (model feature 4), and a non-dimensional threshold which determines when the ice transitions from unbroken to broken (model feature 3).

Lastly, we stress the importance of accurately representing the state of the sea ice. Sea ice forms a crucial barrier between air and sea, and understanding when and how it breaks is crucial to understanding polar regions. As we do not allow for break-up by other mechanisms in this study (e.g., wind or currents), the sea ice break-up here is solely due to the waves. The ability of our model to accurately represent this sea ice break-up thereby substantiates that waves have a critical influence on the morphology of the MIZ, and at very short time scales too.

Conflict of Interest

The authors declare no conflicts of interest relevant to this study.

Data Availability Statement

Observed sea ice concentration has been obtained from ftp://ftp-projects.cen.uni-hamburg.de/seaice/AMSR2. Model simulation data is available for download through the Australian Antarctic Data Centre (https://data.aad.gov.au/metadata/records/AAS_4593_WW3_DavisSea_2020) or through its DOI (https://doi.org/10.26179/e195-t836). Model code and explanation are available at https://github.com/jkousal32/WW3/tree/ice_break_josh.

Acknowledgments
The authors would like to acknowledge Jean Bidlot (European Centre for Medium-Range Weather Forecasts) for the high-resolution wind data, Graig Sutherland (Environment and Climate Change Canada) for the WW3 wave-sea ice attenuation module, and Stefan Zieger (Bureau of Meteorology Australia) for advice on WW3 set up. Josh Kousal appreciates the support of the Australian Government's Research Training Program. Joey J. Voermans, Qingxiang Liu, and Alexander V. Babanin acknowledge support from the Joyce Lambert Antarctic Research Fund and the US Office of Naval Research grant N62909-20-1-2080. Joey J. Voermans, Alexander V. Babanin, and Petra Heil were supported by the Australian Antarctic Program under project 4593 and Petra Heil under project 4506. Open access publishing facilitated by The University of Melbourne, as part of the Wiley - The University of Melbourne agreement via the Council of Australian University Librarians.

References

Ardhuin, F., Otero, M., Merrifield, S., Grouazel, A., & Terrill, E. (2020). Ice breakup controls dissipation of wind waves across Southern Ocean sea ice. *Geophysical Research Letters*, *47*(13), 1–7. https://doi.org/10.1029/2020GL087699

Bateson, A. W., Feltham, D. L., Schröder, D., Hosekova, L., Ridley, J. K., & Aksenov, Y. (2020). Impact of sea ice floe size distribution on seasonal fragmentation and melt of Arctic sea ice. *The Cryosphere*, *14*, 403–428. https://doi.org/10.5194/tc-14-403-2020

Beitsch, A., Kaleschke, L., & Kern, S. (2013). *AMSR2 ASI 3.125 km Sea Ice Concentration Data* (Vol. V01). Institute of Oceanography, University of Hamburg, Germany, digital media.

Boutin, G., Lique, C., Ardhuin, F., Rousset, C., Talandier, C., Accensi, M., & Girard-Ardhuin, F. (2020). Towards a coupled model to investigate wave-sea ice interactions in the Arctic marginal ice zone. *The Cryosphere*, *14*(2), 709–735. https://doi.org/10.5194/tc-14-709-2020

Collins, C. O., Rogers, W. E., Marchenko, A., & Babanin, A. V. (2015). In situ measurements of an energetic wave event in the Arctic marginal ice zone. *Geophysical Research Letters*, *42*, 1–8. https://doi.org/10.1002/2015GL063063

Curry, J. A., Schramm, J. L., & Ebert, E. E. (1995). Sea ice-albedo climate feedback mechanism. *Journal of Climate*, *8*, 240–247. https://doi.org/10.1175/1520-0442(1995)008<0240:siacfm>2.0.co;2

Feltham, D. L. (2005). Granular flow in the marginal ice zone. *Philosophical Transactions of the Royal Society of London A: Mathematical, Physical and Engineering Sciences*, *363*, 1677–1700. https://doi.org/10.1098/rsta.2005.1601

Hasselmann, K., Barnett, T. P., Bouws, E., Carlson, H., Cartwright, D. E., Enke, K., et al. (1973). Measurements of wind-wave growth and swell decay during the Joint north sea wave project (JONSWAP). *Ergaenzungsheft zur Deutschen Hydrographischen Zeitschrift, Reihe A*, *8*(12), 95.

Karulina, M., Marchenko, A., Karulin, E., Sodhi, D., Sakharov, A., & Chistyakov, P. (2019). Full-scale flexural strength of sea ice and freshwater ice in Spitsbergen Fjords and North-West Barents Sea. *Applied Ocean Research*, *90*, 101853. https://doi.org/10.1016/j.apor.2019.101853

Kohout, A. L., & Meylan, M. H. (2008). An elastic plate model for wave attenuation and ice floe breaking in the marginal ice zone. *Journal of Geophysical Research*, *113*(C9). https://doi.org/10.1029/2007jc004434

Langhorne, P. J., Squire, V. A., Fox, C., & Haskell, T. G. (1998). Break-up of sea ice by ocean waves. *Annals of Glaciology*, *27*, 438–442. https://doi.org/10.3189/s0260305500017869

Li, J., Babanin, A. V., Liu, Q., Voermans, J. J., Heil, P., & Tang, Y. (2021). Effects of wave-induced sea ice break-up and mixing in a high-resolution coupled ice-ocean model. *Journal of Marine Science and Engineering*, *9*, 365. https://doi.org/10.3390/jmse9040365

Liu, Q., Babanin, A. V., Rogers, W. E., Zieger, S., Young, I. R., Bidlot, J., et al. (2021). Global wave hindcasts using the observation-based source terms: Description and validation. *Journal of Advances in Modeling Earth Systems*, *13*(8), 1–38. https://doi.org/10.1029/2021ms002493

Liu, Q., Rogers, W. E., Babanin, A. V., Young, I. R., Romero, L., Zieger, S., et al. (2019). Observation-based source terms in the third-generation wave model wavewatch III: Updates and verification. *Journal of Physical Oceanography*, *49*, 489–517. https://doi.org/10.1175/jpo-d-18-0137.1

Longuet-Higgins, M. S. (1977). The mean forces exerted by waves on floating or submerged bodies with applications to sand bars and wave power machines. *Proceedings of the Royal Society of London: Mathematical, Physical and Engineering Sciences*, *352*, 463–480.

Longuet-Higgins, M. S., & Stewart, R. W. (1962). Radiation stresses and mass transport in surface gravity waves with application to 'surf beats'. *Journal of Fluid Mechanics*, *13*, 481–504. https://doi.org/10.1017/s0022112062000877

McPhee, M. G. (1980). An analysis of pack ice drift in summer. *Sea Ice Processes and Models*, 62–75.

Montiel, F., Squire, V. A., & Bennetts, L. G. (2016). Attenuation and directional spreading of ocean wave spectra in the marginal ice zone. *Journal of Fluid Mechanics*, *790*, 492–522. https://doi.org/10.1017/jfm.2016.21

Montiel, F., Squire, V. A., Doble, M., Thomson, J., & Wadhams, P. (2018). Attenuation and directional spreading of ocean waves during a storm event in the Autumn Beaufort sea marginal ice zone. *Journal of Geophysical Research: Oceans*, *123*(8), 5912–5932. https://doi.org/10.1029/2018JC013763

Rabault, J., Sutherland, G., Gundersen, O., Jensen, A., Christensen, K. H., Marchenko, A., & Breivik, Ø. (2020). An open source, versatile, affordable waves in ice instrument for scientific measurements in the polar regions. *Cold Regions Science and Technology*, *170*, 102955. https://doi.org/10.1016/j.coldregions.2019.102955

Rabault, J., Sutherland, G., Jensen, A., Christensen, K. H., & Marchenko, A. (2019). Experiments on wave propagation in grease ice: Combined wave gauges and particle image velocimetry measurements. *Journal of Fluid Mechanics*, *864*, 876–898. https://doi.org/10.1017/jfm.2019.16

Rogers, W. E., Meylan, M. H., & Kohout, A. L. (2021). Estimates of spectral wave attenuation in Antarctic sea ice, using model/data inversion. *Cold Regions Science and Technology*, *182*(3), 103198. https://doi.org/10.1016/j.coldregions.2020.103198

Scientific Committee on Antarctic Research. (2000). *Antarctic Digital database, version 3.0. Database, manual and bibliography. Antarctic Digital database Consortium*.

Shen, H. H., & Ackley, S. (1991). A one-dimensional model for wave-induced ice-floe collisions. *Annals of Glaciology*, *15*, 87–95. https://doi.org/10.1017/s0260305500009587

Squire, V. A. (2020). Ocean wave interactions with sea ice: A reappraisal. *Annual Review of Fluid Mechanics*, *52*, 37–60. https://doi.org/10.1146/annurev-fluid-010719-060301

Steele, M. (1992). Sea ice melting and floe geometry in a simple ice-ocean model. *Journal of Geophysical Research*, *97*, 17729–17738. https://doi.org/10.1029/92jc01755

Stopa, J. E., Sutherland, P., & Ardhuin, F. (2018). Strong and highly variable push of ocean waves on Southern Ocean sea ice. *Proceedings of the National Academy of Sciences*, *115*, 5861–5865. https://doi.org/10.1073/pnas.1802011115

Sutherland, G., Rabault, J., Christensen, K. H., & Jensen, A. (2019). A two layer model for wave dissipation in sea ice. *Applied Ocean Research*, *88*(October), 111–118. https://doi.org/10.1016/j.apor.2019.03.023

Sutherland, P., & Gascard, J.-C. (2016). Airborne remote sensing of ocean wave directional wavenumber spectra in the marginal ice zone. *Geophysical Research Letters*, *43*, 5151–5159. https://doi.org/10.1002/2016GL067713

The WAVEWATCH III Development Group (WW3DG). (2019). *User manual and system documentation of WAVEWATCH III version 6.07. NOAA/NWS/NCEP/MMAB Technical Note*, 333.

Thomson, J., & Rogers, W. E. (2014). Swell and sea in the emerging Arctic ocean. *Geophysical Research Letters*, *41*, 3136–3140. https://doi.org/10.1002/2014gl059983

Timco, G., & Weeks, W. (2010). A review of the engineering properties of sea ice. *Cold Regions Science and Technology*, *60*, 107–129. https://doi.org/10.1016/j.coldregions.2009.10.003

Toffoli, A., Bennetts, L. G., Meylan, M. H., Cavaliere, C., Alberello, A., Elsnab, J., & Monty, J. P. (2015). Sea ice floes dissipate the energy of steep ocean waves. *Geophysical Research Letters*, *42*(20). https://doi.org/10.1002/2015gl065937

Voermans, J. J., Babanin, A. V., Thomson, J., Smith, M. M., & Shen, H. H. (2019). Wave attenuation by sea ice turbulence. *Geophysical Research Letters*, *46*(12), 6796–6803. https://doi.org/10.1029/2019GL082945

Voermans, J. J., Liu, Q., Marchenko, A., Rabault, J., Filchuk, K., Ryzhov, I., et al. (2021). Wave dispersion and dissipation in landfast ice: Comparison of observations against models. *The Cryosphere*, *15*, 5557–5575. https://doi.org/10.5194/tc-15-5557-2021

Voermans, J. J., Rabault, J., Filchuk, K., Ryzhov, I., Heil, P., Marchenko, A., et al. (2020). Experimental evidence for a universal threshold characterizing wave-induced sea ice break-up. *The Cryosphere*, *14*(11), 4265–4278. https://doi.org/10.5194/tc-14-4265-2020

Wadhams, P., Squire, V. A., Ewing, J. A., & Pascal, R. W. (1986). The effect of the marginal ice zone on the directional wave spectrum of the ocean. *Journal of Physical Oceanography*, *16*, 358–376. https://doi.org/10.1175/1520-0485(1986)016<0358:teotmi>2.0.co;2

Wessel, P., & Smith, W. H. F. (1996). A global, self-consistent, hierarchical, high-resolution shoreline database. *Journal of Geophysical Research*, *101*(B4), 8741–8743. https://doi.org/10.1029/96JB00104

Williams, T. D., Rampal, P., & Bouillon, S. (2017). Wave-ice interactions in the neXtSIM sea-ice model. *The Cryosphere Discussions*, *11*(5), 2117–2135. https://doi.org/10.5194/tc-11-2117-2017